Displacement Estimation by Maximum-Likelihood Texture Tracking

Olivier Harant, Lionel Bombrun, *Member, IEEE*, Gabriel Vasile, *Member, IEEE*, Laurent Ferro-Famil, *Member, IEEE*, and Michel Gay, *Member, IEEE*

***Abstract*—This paper presents a novel method to estimate displacement by maximum-likelihood (ML) texture tracking. The observed polarimetric synthetic aperture radar (PolSAR) data-set is composed by two terms: the scalar texture parameter and the speckle component. Based on the Spherically Invariant Random Vectors (SIRV) theory, the ML estimator of the texture is computed. A generalization of the ML texture tracking based on the Fisher probability density function (pdf) modeling is introduced. For random variables with Fisher distributions, the ratio distribution is established. The proposed method is tested with both simulated PolSAR data and spaceborne PolSAR images provided by the TerraSAR-X (TSX) and the RADARSAT-2 (RS-2) sensors.**

***Index Terms*—Maximum-likelihood (ML), offset tracking, polarimetric synthetic aperture radar (SAR), spherically invariant random vectors, texture.**

I. Introduction

GLACIER monitoring is a widely common problem which is investigated for years. The progressive awareness to climate changes makes these investigations more and more required as the glaciers are good indicators for local climate variation.

Different approaches using both optical and SAR sensors have been proposed to derive displacement fields. In the optical domain, optical flow methods have been successfully validated [1], but those methods are strongly dependent by weather phenomenon (snow fall, etc.) which will change the scene illumination. In addition, optical flow methods required cloudless images. Because of its all weather and all-day monitoring capabilities, SAR imagery offers a number of advantages for Earth-surface and feature observation. Different approaches have been proposed to derive displacement fields with SAR imagery: Differential Interferometric SAR (D-InSAR) and offset tracking techniques.

Although the potential of D-InSAR methods [2] have been successfully validated on different geophysical objects such as volcanoes, landslides [3], glaciers [4]–[7], its application is limited to coherence preservation. For the generation of new high resolution sensors (RADARSAT-2, TSX), the repeat time observation intervals becomes larger. It varies from 11 days for TSX to 24 days for RADARSAT-2 compared to 1 day during the ERS-1/2 tandem mission. For TSX data, coherence is not preserved at 11 days in winter on Alpine glaciers [8]. Another limitation of D-InSAR techniques concerns the fact that the displacement estimated is only a projection in the line-of-sight (LOS) direction. Different hypothesis have been proposed to retrieve the three components. A common assumption is to consider a flow parallel to the glacier surface and in the direction of maximum averaged downhill slope [7]. Another approach is to combine both ascending and descending passes [9].

Nevertheless, the new generation of recently launched SAR sensors are now able to produce high quality images of the Earth's surface with meter resolution. The decrease of the resolution cell offers the opportunity to observe much thinner spatial features. Offset tracking methods in the SAR domain are now more and more studied. It exists different techniques:

- The **speckle tracking** technique correlates small blocks to determine the relative displacement in the range and azimuth (along-track) directions [10] [11]. This technique does not depend on image feature tracking but rather on the fact that there is coherence between the blocks. As coherence is not preserved with TSX for temperate Alpine glaciers, the speckle tracking method is not well suited.
- Recently, a novel tracking method based on **Isolated Point Scatterer** (IPS) has been proposed [12]. It corresponds to the matched filter between the signal backscattered by an IPS and the ideal response: a double cardinal sinus. This method is valid only for particular objects such as corner reflector.
- The classical **intensity tracking** technique based on the normalized cross-correlation (NCC) criterion [13] [14].
- The **Maximum-Likelihood (ML) texture tracking** algorithm which takes into account the statistics of the backscattered signal [15].

In this paper, authors propose an algorithm closed to the ML texture tracking algorithm introduced by Erten *et al.* [15]. It takes into accounts the statistics of the texture parameter extracted from the PolSAR data. Fig. 1 shows the global scheme of this method.

Manuscript received April 20, 2010; revised November 17, 2010; accepted November 28, 2010. Date of publication December 17, 2010; date of current version May 18, 2011. This work was supported by the French Research Agency (ANR) through the EFIDIR Project (ANR-2007-MCDC0-04, The associate editor coordinating the review of this manuscript and approving it for publication was Prof. Jocelyn Chanussot.

O. Harant is with the GIPSA-Lab, CNRS INPG-961, 46-38402 Saint-Martin-d'Hères, France, and also with the IETR Laboratory, SAPHIR Team, University of Rennes 1, 35042 Rennes, France (e-mail: olivier.harant@gipsa-lab.grenoble-inp.fr).

L. Bombrun, G. Vasile, and M. Gay are with the GIPSA-Lab, CNRS INPG-961, 46-38402 Saint-Martin-d'Hères, France (e-mail: lionel.bombrun@gipsa-lab.grenoble-inp.fr; gabriel.vasile@gipsa-lab.grenoble-inp.fr; michel.gay@gipsa-lab.grenoble-inp.fr).

L. Ferro-Famil is with the IETR Laboratory, SAPHIR Team, University of Rennes 1, 35042 Rennes, France (e-mail: laurent.ferro-famil@univ-rennes1.fr).

Color versions of one or more of the figures in this paper are available online at http://ieeexplore.ieee.org.

Digital Object Identifier 10.1109/JSTSP.2010.2100365

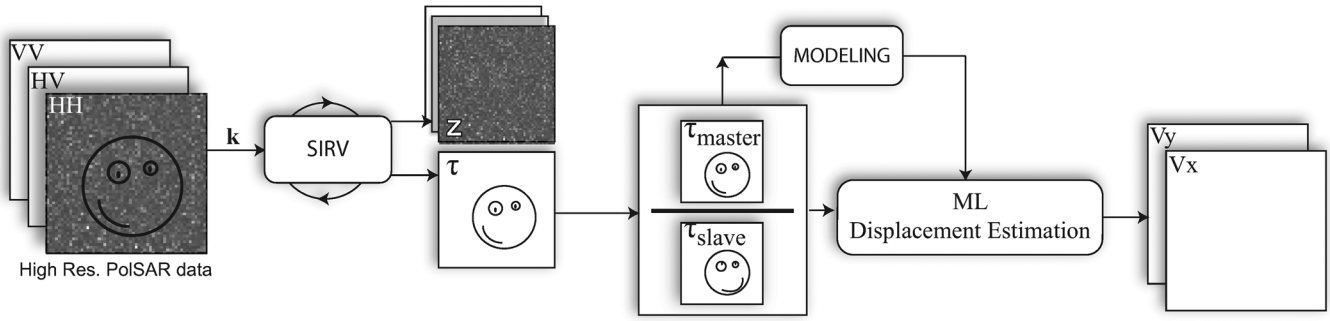

Fig. 1. Global scheme of the generalized ML texture tracking method.

This paper is organized as follows. In Section II, the Spherically Invariant Random Vectors (SIRV) model is introduced to extract the texture component from PolSAR data. Next, we focus on the texture modeling. Then, in Section III, the ML texture tracking algorithm is presented and adapted to the proposed texture model with both uncorrelated and correlated texture between images. Section IV presents results on simulated data, on dual-pol TSX and quad-pol RADARSAT-2 data over the Argentière glacier. Finally, some conclusion and perspectives of this work are discussed.

II. SIRV Model

A. Principle

With the new generation of airborne and spaceborne SAR sensors, the number of scatterers present in each resolution cell decreases considerably, homogeneous hypothesis of the PolSAR clutter can be reconsidered. Heterogeneous clutter models have therefore recently been studied with POLSAR data with the SIRV processes [16].

From a PolSAR point of view, the target vector $\mathbf{k}$ can be defined as the product of a square root of a positive random variable τ (representing the texture) with an independent complex Gaussian vector $\mathbf{z}$ with zero mean and covariance matrix $[M] = E\{\mathbf{z}\mathbf{z}^H\}$ (representing the speckle):

$$\mathbf{k} = \sqrt{\tau}\,\mathbf{z} \tag{1}$$

where the superscript H denotes the complex conjugate transposition and $E\{\cdot\}$ the mathematical expectation.

B. SIRV Estimation Scheme

For a given covariance matrix $[M]$, the ML estimator of the texture parameter τ for the pixel i ($\hat{\tau}_i$) is given by

$$\hat{\tau}_i = \frac{\mathbf{k}_i^H [M]^{-1} \mathbf{k}_i}{p} \tag{2}$$

where p is the dimension of the target scattering vector $\mathbf{k}$ ($p = 3$ for the reciprocal case).

The ML estimator of the normalized covariance matrix under the deterministic texture case is the solution of the following recursive equation:

$$[\hat{M}]_{FP} = f\left([\hat{M}]_{FP}\right) = \frac{p}{N}\sum_{i=1}^{N} \frac{\mathbf{k}_i \mathbf{k}_i^H}{\mathbf{k}_i^H [\hat{M}]_{FP}^{-1} \mathbf{k}_i} = \frac{p}{N}\sum_{i=1}^{N} \frac{\mathbf{z}_i \mathbf{z}_i^H}{\mathbf{z}_i^H [\hat{M}]_{FP}^{-1} \mathbf{z}_i}. \tag{3}$$

In the random texture τ case, the ML estimator of the normalized covariance matrix depends on the texture pdf $p_\tau(\tau)$ and is given by [17]

$$[\hat{M}_{ML}] = \frac{1}{N}\sum_{i=1}^{N} \frac{h_{p+1}\left(\mathbf{k}_i^H [\hat{M}_{ML}]^{-1} \mathbf{k}_i\right)}{h_p\left(\mathbf{k}_i^H [\hat{M}_{ML}]^{-1} \mathbf{k}_i\right)} \mathbf{k}_i \mathbf{k}_i^H \tag{4}$$

where $h_p(x)$ is the density generator function defined by [18] [19]

$$h_p(x) = \int_0^{+\infty} \frac{1}{\tau^p} \exp\left(-\frac{x}{\tau}\right) p_\tau(\tau)\, d\tau. \tag{5}$$

For sake of simplicity and computational efficiency, this study is limited to the "approximate" ML estimator (3). Pascal *et al.* have established the existence and the uniqueness, up to a scalar factor, of the Fixed Point estimator of the normalized covariance matrix, as well as the convergence of the recursive algorithm whatever the initialization [20] [21]. In this paper, the trace of the covariance matrix is normalized to p the dimension of target scattering vector. In practice, the normalized covariance matrix is first computed because it does not depend on the texture component. Then, the ML estimator of the texture parameter is estimated according to (2).

It is important to notice that in the SIRV definition, the probability density function (pdf) of the texture random variable is not explicitly specified. As a consequence, SIRVs describe a whole class of stochastic processes. This class includes the conventional clutter models having Gaussian, $\mathcal{K}$, $\mathcal{G}^0$, KummerU pdfs which correspond respectively to Dirac, Gamma, Inverse Gamma, and Fisher distributed texture [22]–[24].

C. Texture Modeling

1) Fisher pdf: The Fisher pdf is the Pearson type VI distribution, it is defined by three parameters as [25]–[27]

$$p_\tau(\tau) = \mathcal{F}[m, \mathcal{L}, \mathcal{M}] = \frac{\Gamma(\mathcal{L}+\mathcal{M})}{\Gamma(\mathcal{L})\Gamma(\mathcal{M})} \frac{\mathcal{L}}{\mathcal{M}m} \frac{\left(\frac{\mathcal{L}\tau}{\mathcal{M}m}\right)^{\mathcal{L}-1}}{\left(1+\frac{\mathcal{L}\tau}{\mathcal{M}m}\right)^{\mathcal{L}+\mathcal{M}}} \tag{6}$$

with $\mathcal{L} > 0$ and $\mathcal{M} > 0$.

As Fisher pdfs can be viewed as the Mellin convolution of a Gamma pdf by an Inverse Gamma pdf [26], they can fit distributions with either heavy heads or heavy tails.

2) Benefit of Fisher PDF: A glacier area (80 × 35 pixels) from the X-band TSX data over the Chamonix Mont-Blanc test-

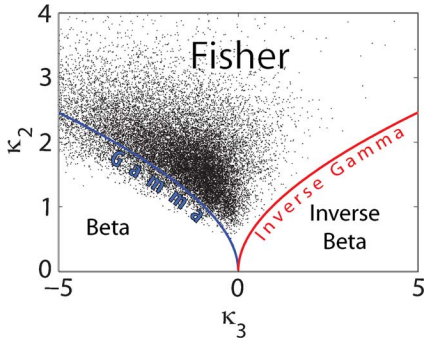

Fig. 2. κ_2/κ_3 plan for a glacier area over the Chamonix Mont-Blanc test-site (TSX, X-band).

site has been extracted. Then, the covariance matrix $[M]_{FP}$ and the texture parameter τ are estimated according to (2) and (3). To see the benefit of Fisher pdfs to model the texture of PolSAR data, the κ_2/κ_3 plan has been plotted in Fig. 2. It shows the evolution of the second log-cumulant κ_2 versus the third log-cumulant κ_3. In this plan, Gamma and Inverse Gamma pdf are respectively represented by the blue and red lines. The first three log-cumulants estimates are

$$\begin{aligned}\hat{\kappa}_1 &= \frac{1}{N}\sum_{i=1}^{N}\ln\tau_i \\ \hat{\kappa}_2 &= \frac{1}{N}\sum_{i=1}^{N}(\ln\tau_i - \hat{\kappa}_1)^2 \\ \hat{\kappa}_3 &= \frac{1}{N}\sum_{i=1}^{N}(\ln\tau_i - \hat{\kappa}_1)^3\end{aligned} \tag{7}$$

where N is the number of pixels in the sliding window. In the case of Fig. 2, a 7×7 pixels sliding window has been used to compute the log-cumulants. Fisher pdfs cover all the space between the blue and red line [25].

In this example, 15.53% of the pixels are Beta distributed (under the blue line), 0.004% are Inverse Beta distributed (under the red line) and 84.47% are Fisher distributed. It shows that Fisher pdfs are well adapted to model PolSAR clutter [24]. In the following, the texture parameter will be considered to be Fisher distributed.

After having shown the benefit of Fisher pdfs to model the texture of high-resolution PolSAR data, we propose to implement this distribution in the ML texture tracking algorithm. As Fisher pdfs are a generalization of Gamma pdfs, the proposed algorithm can be seen as an extension of the algorithm proposed by Erten *et al.* [15].

III. Texture Tracking

A. Principle

Classical algorithms estimate the shift between images by maximizing the normalized cross-correlation coefficient. This criterion is the ML solution for optical data corrupted by additive noise [28] or for complex SAR data having circular Gaussian statistics [29]. With increasing the resolution of PolSAR data, the number of scatterers in each resolution decreases. The central limit theorem may not be respected and the Gaussian hypothesis may be reconsidered. Consequently, the NCC criterion may not be optimal for high-resolution PolSAR data. In this section, the texture tracking algorithm is improved based on the SIRV model and the Fisher distribution for texture modeling.

Let $\mathbf{k}_y^i = [\mathbf{k}_{y_1}^i, \ldots, \mathbf{k}_{y_k}^i]$ and $\mathbf{k}_x = [\mathbf{k}_{x_1}, \ldots, \mathbf{k}_{x_k}]$ be two blocks of the PolSAR data-set containing k pixels. They represent respectively the slave and master images. According to (2) and (3), the texture blocks $\tau_y^i = [\tau_{y_1}^i, \ldots, \tau_{y_k}^i]$ and $\tau_x = [\tau_{x_1}, \ldots, \tau_{x_k}]$ are estimated. The slave block i is shifted from the master one with a displacement $\mathbf{v}_i$. In this study, the vector $\mathbf{v}_i$ is limited to a translation and has only two components $[v_i{}^d, v_i^{az}]$ in range and azimuth. The ML texture tracking algorithm estimates the shift vector $\mathbf{v}_{\mathrm{ML}}$ by maximizing for each slave block i the conditional density function (cdf) [15]. It yields

$$\mathbf{v}_{\mathrm{ML}} = \underset{i}{\mathrm{Argmax}}\ p\left(\tau_x | \tau_y^i, \mathbf{v}_i\right). \tag{8}$$

By following the same procedure as described in [15], the pdf of the texture ratio $\alpha = \tau_x/\tau_y$ must be established to estimate the shift vector. This study has to be done when the texture between images is uncorrelated and correlated.

B. Texture Model With Uncorrelated Texture Between Images

If τ_x and τ_y are two independent and identically distributed (i.i.d.) random variables, the pdf of the texture ratio α is given by [30, Eq. 6.56]

$$p_\alpha(\alpha) = \int_0^\infty p_{\tau_x}(\alpha\tau)p_{\tau_y}(\tau)\tau d\tau. \tag{9}$$

For Fisher distributed texture, the pdf of the ratio of two uncorrelated texture has been established (see Appendix A), its expression is given by

$$\begin{aligned}p_\alpha(\alpha) = &\frac{B(2\mathcal{L}, 2\mathcal{M})}{[B(\mathcal{L}, \mathcal{M})]^2}\frac{1}{\alpha^{\mathcal{M}+1}} \\ &\times {}_2F_1\left(\mathcal{L}+\mathcal{M}, 2\mathcal{M}; 2(\mathcal{L}+\mathcal{M}); \frac{\alpha-1}{\alpha}\right)\end{aligned} \tag{10}$$

where ${}_2F_1(\cdot,\cdot;\cdot;\cdot)$ and $B(\cdot,\cdot)$ are respectively the Gauss hypergeometric function and the Euler Beta function ($B(z,w) = \Gamma(z)\Gamma(w)/\Gamma(z+w), \Re\mathrm{e}(z) \geq 0, \Re\mathrm{e}(w) \geq 0$). $\mathcal{L}$ and $\mathcal{M}$ are the two shape parameters of the Fisher pdf. The scale parameter m simplifies because the texture ratio variable is studied.

According to [15], (8) is equivalent to

$$\mathbf{v}_{\mathrm{ML}} = \underset{i}{\mathrm{Argmax}} \prod_{j=1}^{k} \frac{1}{\tau_{y_j}^i}\, p_\alpha\left(\frac{\tau_{x_j}}{\tau_{y_j}^i}\right). \tag{11}$$

It yields

$$\begin{aligned}\mathbf{v}_{\mathrm{ML}} = \underset{i}{\mathrm{Argmax}} &\prod_{j=1}^{k} \frac{B(2\mathcal{L}, 2\mathcal{M})}{[B(\mathcal{L}, \mathcal{M})]^2}\frac{1}{\tau_{y_j}^i}\left(\frac{\tau_{x_j}}{\tau_{y_j}^i}\right)^{-1-\mathcal{M}} \\ &\times {}_2F_1\left(\mathcal{L}+\mathcal{M}, 2\mathcal{M}; 2(\mathcal{L}+\mathcal{M}); 1-\frac{\tau_{y_j}^i}{\tau_{x_j}}\right).\end{aligned} \tag{12}$$

By taking the natural logarithm of (12), one can prove that the criterion to maximize to estimate the shift vector for uncorrelated texture between images is

$$\mathrm{L}(\mathbf{v}_i) = k \ln \left(\frac{B(2\mathcal{L}, 2\mathcal{M})}{[B(\mathcal{L}, \mathcal{M})]^2} \right) + \mathcal{M} \sum_{j=1}^{k} \ln \frac{\tau_{y_j}^i}{\tau_{x_j}} - \sum_{j=1}^{k} \ln \tau_{x_j}^i + \sum_{j=1}^{k} \ln \left({}_2F_1 \left(\mathcal{L} + \mathcal{M}, 2\mathcal{M}; 2(\mathcal{L} + \mathcal{M}); 1 - \frac{\tau_{y_j}^i}{\tau_{x_j}} \right) \right). \quad (13)$$

C. Texture Model With Correlated Texture Between Images

In the case of correlated texture between two images, the bivariate Fisher distribution with marginal Fisher pdf should be used. Its pdf is defined by six parameters as [31]

$$\begin{aligned} p_{X_1,X_2}(x_1, x_2) &= \frac{R_1^{\mathcal{L}_1} R_2^{\mathcal{L}_2}}{B(\mathcal{L}_1, \mathcal{M}_1) B(\mathcal{L}_2, \mathcal{L}_1 + \mathcal{M}_2)} \\ &\quad \times x_1^{\mathcal{L}_1 - 1} x_2^{\mathcal{L}_2 - 1} (1 + R_1 x_1 + R_2 x_2)^{-(\mathcal{L}_1 + \mathcal{L}_2 + \mathcal{M}_2)} \\ &\quad \times {}_2F_1(\mathcal{L}_1 + \mathcal{L}_2 + \mathcal{M}_2, \mathcal{M}_2 - \mathcal{M}_1; \mathcal{L}_1 + \mathcal{M}_2; w) \end{aligned} \quad (14)$$

with $R_1 = \mathcal{L}_1/\mathcal{M}_1 m_1$, $R_2 = \mathcal{L}_2/\mathcal{M}_2 m_2$ and $w = R_1 x_1/1 + R_1 x_1 + R_2 x_2$.

For Fisher distributed texture, the pdf of the ratio of two correlated texture has been established (see Appendix B), its expression is given by

$$p_\alpha(\alpha) = \frac{R_1^{\mathcal{L}_1} R_2^{\mathcal{L}_2}}{B(\mathcal{L}_1, \mathcal{M}_1)} \frac{B(\mathcal{L}_1 + \mathcal{L}_2, \mathcal{M}_2)}{B(\mathcal{L}_2, \mathcal{L}_1 + \mathcal{M}_2)} \frac{\alpha^{\mathcal{L}_1 - 1}}{(R_1 \alpha + R_2)^{\mathcal{L}_1 + \mathcal{L}_2}} \times {}_2F_1(\mathcal{L}_1 + \mathcal{L}_2, \mathcal{M}_2 - \mathcal{M}_1; \mathcal{L}_1 + \mathcal{M}_2; z) \quad (15)$$

with $z = 1/1 + (R_2/R_1)(1/\alpha)$.

By following the same procedure as described in Section III-B, the criterion to maximize to estimate the shift vector for correlated texture between images is given by

$$\begin{aligned} \mathrm{L}(\mathbf{v}_i) &= K + (\mathcal{L}_1 - 1) \sum_{j=1}^{k} \ln \tau_{x_j} + (\mathcal{L}_2 + 1) \sum_{j=1}^{k} \ln \tau_{y_j}^i \\ &\quad - (\mathcal{L}_1 + \mathcal{L}_2) \sum_{j=1}^{k} \ln \left(R_1 \tau_{x_j} + R_2 \tau_{y_j}^i \right) \\ &\quad + \sum_{j=1}^{k} \ln \left({}_2F_1(\mathcal{L}_1 + \mathcal{L}_2, \mathcal{M}_2 - \mathcal{M}_1; \mathcal{L}_1 + \mathcal{M}_2; z) \right) \end{aligned} \quad (16)$$

with $K = k(\ln R_1^{\mathcal{L}_1} + \ln R_2^{\mathcal{L}_2}) + k \ln(B(\mathcal{L}_1 + \mathcal{L}_2, \mathcal{M}_2)/B(\mathcal{L}_1, \mathcal{M}_1) B(\mathcal{L}_2, \mathcal{L}_1 + \mathcal{M}_2))$.

In (16), the term $R_1 \tau_{x_j} + R_2 \tau_{y_j}^i$ depends on the samples order. It plays a role similar as the cross-correlation coefficient which takes into account the spatial arrangement of pixels.

IV. Results

A. On Simulated Data

Simulations have been performed to test the reliability of the ML shift estimators. One Master/Slave image pair is sampled from the same Fisher pdf for each region. The master and slave images are shaped according to a 2-D rectangular function. The border is sampled from $\mathcal{F}[1, 2, 0.5]$. The center is sampled from $\mathcal{F}[5, 6, 0.8]$ and corresponds to the size of the estimation neighborhood. The simulated dataset has been corrupted with independent multiplicative noise sampled from a Gamma pdf $\mathcal{G}[1, 1]$. Fig. 3(a) shows an example of one simulation.

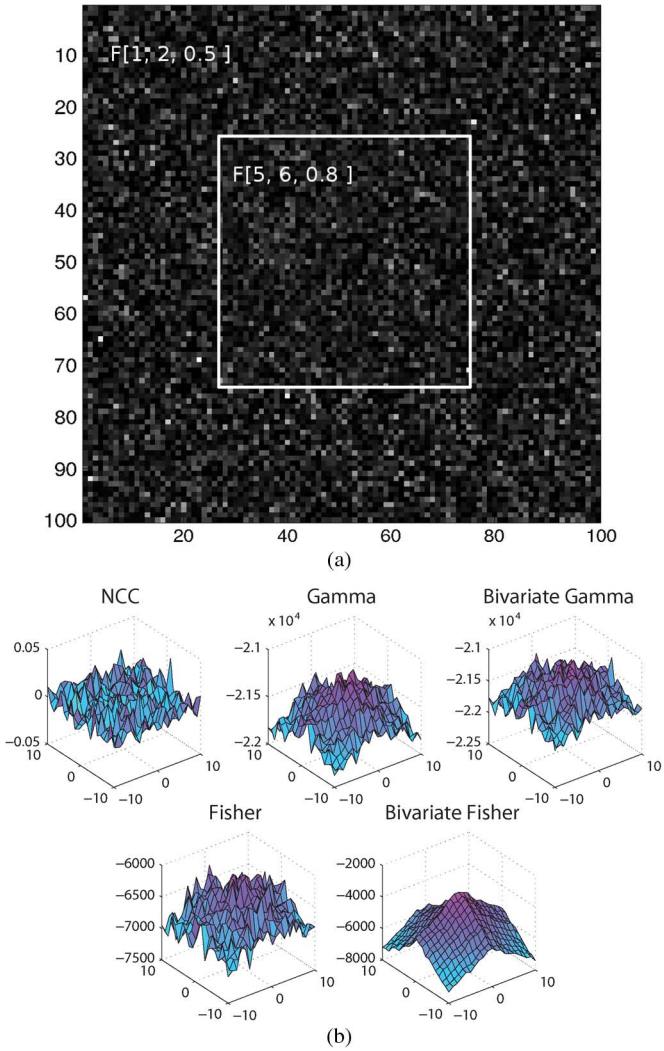

Fig. 3. NCC, uncorrelated and correlated Gamma ML, uncorrelated and correlated Fisher ML criteria computed on simulations. (a) Simulated texture data. (b) Detection surfaces for the multiplicative noised dataset: NCC, uncorrelated and correlated Gamma ML, uncorrelated and correlated Fisher ML.

Five shift estimators are then computed: NCC, uncorrelated and correlated Gamma ML, uncorrelated and correlated Fisher ML. Since there is no motion between the two texture images, the detection surface should be flat except in the center, where a peak is expected.

Fig. 3(b) illustrates the results obtained where 1000 Monte Carlo simulations have been performed for the shift estimators (NCC and MLs). The NCC, both uncorrelated and correlated Gamma ML and the uncorrelated Fisher ML estimators fail to detect the no-motion: the criteria are very noisy without any peak. However, the correlated Fisher ML gives a smoother detection surface with a more pronounced detection peak. This recommends the correlated Fisher ML texture tracking with multiplicative noise.

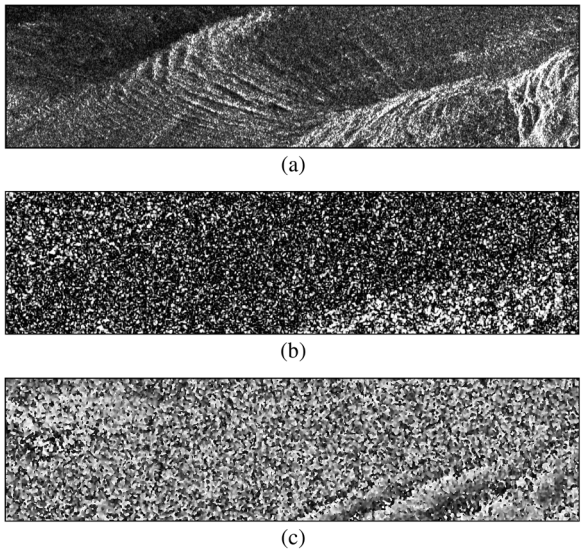

Fig. 4. D-InSAR results from 2009-01-06/2009-01-17 couple. (a) Amplitude. (b) Coherence. (c) Phase images.

B. On Real Data

1) Argentière Glacier Test-Site: This work introduces some preliminary TSX and RADARSAT-2 observations of the Argentière glacier in order to estimate its displacement. It is located in the Mont-Blanc massif, its head (catchment area) starts near 3000 m. Its slope is quite regular and not steep except at the bottom where the seracs fall breaks the slope and disconnects the terminal part from the rest of the glacier. 14 TSX and 4 RADARSAT-2 images have been acquired on the Argentière glacier during the winter and spring 2008–2009.

2) D-InSAR Potential: As the surface of the temperate glacier changes from one day to another, in the TSX case and more generally at X-band, the interferometry on the surface of temperate glaciers is difficult and its potential is quite limited [8]. Fig. 4 shows amplitude, coherence and phase of an 11-day interferogram acquired in winter (2009-01-06/2009-01-17). For this interferometric couple, coherence is not preserved on the Argentière glacier. The interferometric phase cannot be used to derive displacement fields.

3) Texture Tracking: As the new sensors provide higher resolution and according to the limitation of the interferometric methods on the temperate glaciers, incoherent methods seems promising. From October 2007 to June 2009, 14 TSX complex dual-pol images in stripmap mode and 4 RADARSAT-2 complex fine quad-pol images have been acquired over the Chamonix Mont-Blanc test-site. Table I summaries the main details of the two images pairs on which we have worked. Only a coarse coregistration has been processed in each images pair to avoid any distortion which could affect the polarimetric and statistical properties. The subpixel coregistration values should be subtracted to the texture tracking results.

a) On TSX data: Fig. 5 shows the displacement field derived over one crevasses area of the Argentière glacier. The texture image pair is extracted using the SIRV estimation scheme [16]. A 64 × 256 pixels sliding window has been used to derive the displacement map. As expected, the displacement on the

TABLE I
DETAILS OF TSX AND RADARSAT-2 PRODUCTS

Prod.	Date	Pixel Spacing Rng × Az	Polarizations	Inc. angle
TSX	2009-01-06 2009-02-08	1.4m × 2.5m	HH / HV	37.8°
RS-2	2009-01-29 2009-02-22	4.7m × 5.1m	HH / HV / VV	31.5°

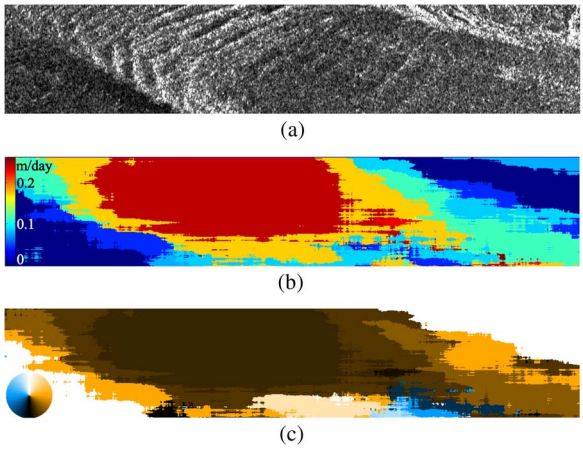

Fig. 5. Displacement estimation over a crevasse field of the Argentière glacier, dual-pol TSX data, 2009-01-06/2009-02-08. (a) Master texture estimated using SIRV model. (b) Displacement field in LOS. (c) Orientation map.

border of the glacier is closed to zero. Note that the mean displacement over the crevasse field is about two times higher than over the homogeneous area of the glacier. This corresponds to the annual displacement estimation provided by glaciologists.[1] Further studies need to quantitatively assess the derived shift estimates.

Note also that orientation of the motion field is consistent with the conventional temperate glacier flow model: from the upper left to the bottom right of the image.

Contrary to the NCC criterion, the confidence interval for the ML similarity measure is hard to qualify. Further investigations should be necessary to derive the false alarm probability for Fisher distributed texture. In [15], Erten *et al.* have introduced the following $\mathcal{Q}_{ML}$ index defined by

$$\mathcal{Q}_{ML} = \frac{\max(ML) - \text{mean}(ML)}{\text{mean}(ML) - \min(ML)}. \tag{17}$$

$\mathcal{Q}_{ML}$ is a measure of confidence. The higher is $\mathcal{Q}_{ML}$, the more accurate is the displacement estimation.

Table II shows the mean and variance of two samples extracted respectively from a crevasses area and an homogeneous area of the glacier. The mean of $\mathcal{Q}_{ML}$ is higher on crevasses area and its variance is lower. It highlights the sensitivity of the ML criterion to the texture heterogeneity. Reliable displacement results are obtained on the crevasses areas.

b) Regularisation: For the study of geophysical objects, *a priori* flow model can be added to similarity measure to estimate

[1]LGGE. Glacioclim.

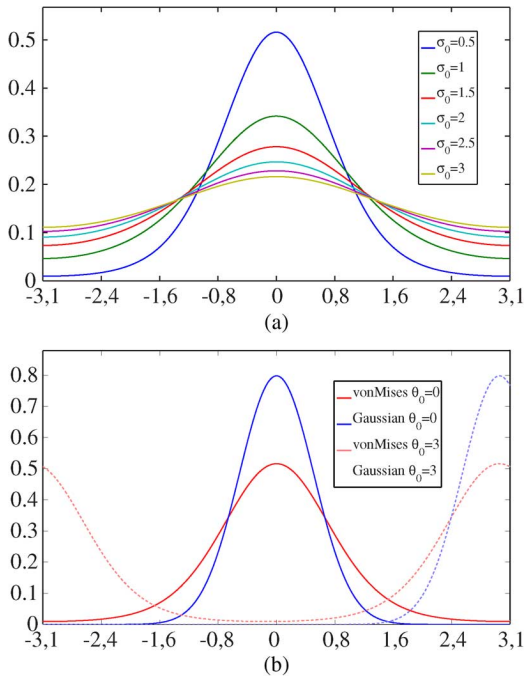

Fig. 6. von Mises pdf is the circular analogue of the normal distribution. (a) von Mises pdf. $\theta_i^0 = 0$. (b) Normal and von Mises pdfs. $\sigma_i^0 = 0.5$. $\theta_i^0 \neq 0$: circularity of the von Mises pdf on $-\pi, +\pi$.

TABLE II
$\mathcal{Q}_{ML}$ MEAN AND VARIANCE OVER TWO AREAS ON THE ARGENTIÈRE GLACIER COMPUTED FROM TSX DATA

$\mathcal{Q}_{ML}$	Crevasses area	Homogeneous area
Mean	1.2858	0.9224
Variance	0.2470	0.0728

the displacement field. According to Bayes' rule, the problem formulation becomes

$$p\left(\tau_y^i, \mathbf{v}_i | \tau_x^i\right) = \frac{p\left(\tau_x^i | \tau_y^i, \mathbf{v}_i\right) p\left(\tau_y^i | \mathbf{v}_i\right) p(\mathbf{v}_i)}{p\left(\tau_x^i\right)}. \quad (18)$$

Let v_i^d and v_i^{az} be, respectively, the two components of the displacement vector $\mathbf{v}_i$ along the distance and azimuth direction. In (18), the prior term $p(\mathbf{v}_i)$ can be rewritten as

$$p(\mathbf{v}_i) = p_\rho(\rho_i)\, p_\theta(\theta_i) \quad (19)$$

where ρ_i and θ_i are the polar coordinates of the displacement vector $\mathbf{v}_i$. They are linked with the distance and azimuth component by $\rho_i = \sqrt{{v_i^d}^2 + {v_i^{az}}^2}$ and $\theta_i = \text{atan}(v_i^{az}/v_i^d)$.

For the Argentière glacier, the assumptions of a flow parallel to the glacier surface and in the direction of the maximum downhill slope have been successfully validated with *in situ* measurements [7]. Those information can be included in the prior model. Consequently, the orientation angle θ_i is assumed to be normally distributed and having circular values between $-\pi$ and $+\pi$. This parameter follows the *von Mises* distribution (also known as the circular normal distribution) which is the circular analog of the normal distribution [32] (Fig. 6)

$$p_\theta(\theta_i) = \frac{1}{2\pi I_0\left(\frac{1}{\sigma_i^0}\right)} \exp\left(\frac{1}{\sigma_i^0} \cos\left(\theta_i - \theta_i^0\right)\right) \quad (20)$$

with θ_i^0 mean and σ_i^0 standard deviation. θ_i^0 is the direction in the maximum downhill slope issued from a digital elevation model. σ_i^0 is fixed here to π. $I_0(.)$ is the modified Bessel function of order 0. Concerning the absolute value of the displacement ρ_i, no constraint is imposed. ρ_i is therefore assumed to be uniformly distributed in the search neighborhood.

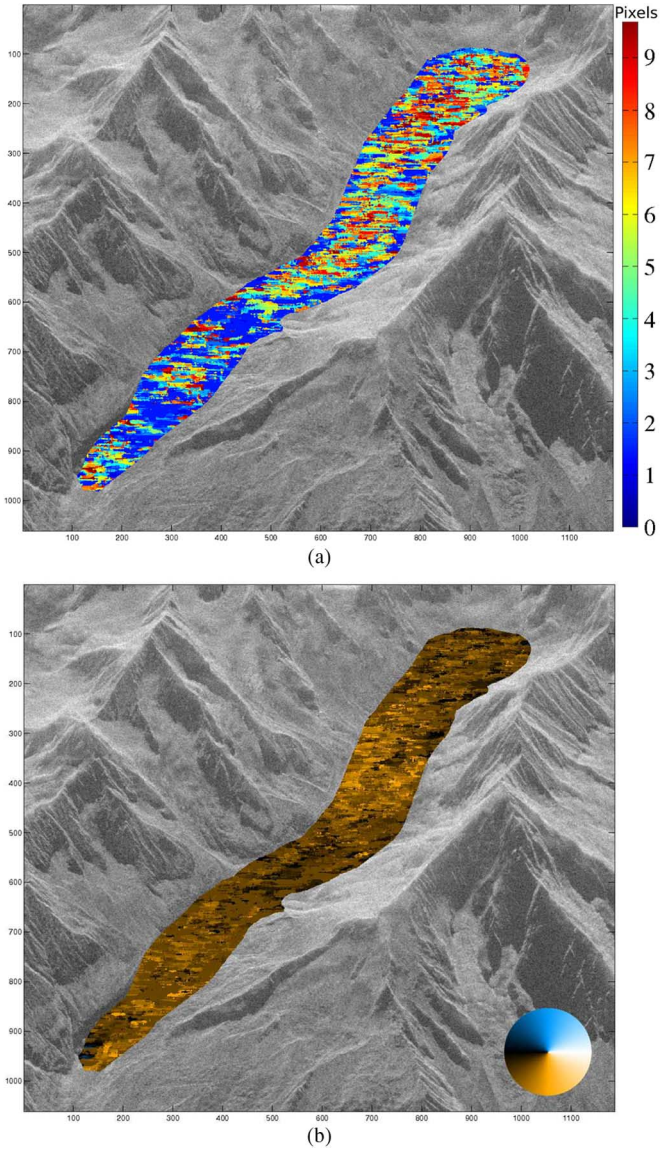

Fig. 7. Displacement estimation over the Argentière glacier with regularisation according to Bayes' rule, quad-pol RADARSART-2 data, 2009-01-29/2009-02-22. (a) Displacement field in LOS. (b) Orientation map.

c) On RADARSAT-2 data: Fig. 7 illustrates a displacement estimation using quad-pol RADARSAT-2 data. On this example, a regularization process has been applied according to a Bayes' rule formulation. The orientation map has been extracted from a DEM of the Mont-Blanc massif with a resolution

of 10 m and projected in SAR geometry. As expected, the orientation map [Fig. 7(b)] is consistent with the glacier flow model.

V. Discussion

In this paper, the study has been focused on the generalization of the ML texture tracking using the Fisher pdfs which have the ability to fit a wide range of texture scenes. For glacier texture tracking, we recommend to use low-frequency bands as the C-band or less to penetrate under the dry snow. This will permit to observe structures (dust, eratic blocks, relief, etc.) present on the ice surface which is more heterogeneous and more stable in time than the snow.

In this paper, the ML texture tracking algorithm has been applied on Alpine glaciers. They present the advantage to have large displacement. Nevertheless, their surface is quite homogeneous and does not highlight the benefit of Fisher pdfs for texture modeling. This kind of method can be relevant for the monitoring of other geophysical objects such as volcanoes, earthquakes, etc., which have rough surfaces. The more heterogeneous the ground is and/or the higher the resolution is, the more relevant the texture information is for displacement estimation, segmentation and denoising.

Many recent works have been dedicated to the statistical modeling of the backscattering signal. For this purpose, Mellin transform and second kind statistics define a well-suited formalism [27]. In this context, many distributions have been introduced as a generalization of the well-known Gamma pdf. Here, the 3-parameter Fisher pdf has been used but other statistics such as the KWBU pdfs system may be considered [33]. Those 4-parameter distributions should permit a better texture modeling. Further investigations still remains necessary to quantify the benefit of models with more freedom degrees.

VI. Conclusion

With the new generation of launched PolSAR sensors, the Earth's surface is imaged with meter resolution. Small spatial features can then be observed from the space. Recently, more and more studies are dedicated to texture extraction and modeling. Based on this consideration, this paper has presented a new texture tracking method to derive displacement fields from PolSAR data. According to the SIRV estimation scheme, the texture parameter can be estimated and isolated from the speckle component. The proposed algorithm estimates a shift vector through maximizing the cdf of two matched texture blocks.

Due to their capability to fit distributions with either heavy heads or heavy tails, Fisher pdfs are well adapted to model the texture variable. This observation has been illustrated on real PolSAR data. Next, based on the assumption of Fisher distributed texture, the pdfs of the ratio of two texture variables have been established for both uncorrelated and correlated texture between images. Then, a ML criterion has been established to measure the similarity between two blocks: one for the master and one for the slave texture images. This similarity measure is computed in a neighborhood of the slave image. The shift vector which leads to the largest log-likelihood value yields to the estimated displacement.

Then, the ML texture tracking algorithm has been applied on simulated and real PolSAR data. The proposed algorithm has been compared to the NCC criterion and the ML tracking algorithm based on Gamma assumption for the texture component.

Contrary to the NCC criterion, the confidence interval for the ML similarity measure is hard to qualify. Further investigations should be necessary to derive the false alarm probability for Fisher distributed texture.

As discussed before, the ML texture tracking confidence interval is hard to be qualify. Erten *et al.* have introduced the $\mathcal{Q}_{ML}$ factor which provides some information on the behavior of the ML distribution. Nevertheless, some works are necessary to define the PFA for the ML criteria. This will permit to threshold the similarity image and conclude or not on the relevance of the results.

Further works will deal with the addition of the covariance matrix information to estimate displacement. Indeed, only the texture variable is used in the ML tracking algorithm. The polarimetric diversity contains very useful information concerning the scattering mechanisms. This type of information has been widely used in classification of PolSAR data. It should probably improve tracking performances.

Appendix A

This appendix gives the mathematical details of the pdf of α for uncorrelated Fisher distributed texture. In such case, the pdf of α is obtained by replacing the expression of the Fisher pdf (6) in (9), it yields

$$\begin{aligned} p_\alpha(\alpha) &= \int_0^\infty \frac{\Gamma(\mathcal{L}+\mathcal{M})}{\Gamma(\mathcal{L})\Gamma(\mathcal{M})}\frac{\mathcal{L}}{\mathcal{M}m}\frac{\left(\frac{\mathcal{L}\alpha\tau}{\mathcal{M}m}\right)^{\mathcal{L}-1}}{\left(1+\frac{\mathcal{L}\alpha\tau}{\mathcal{M}m}\right)^{\mathcal{L}+\mathcal{M}}} \\ &\quad\times \frac{\Gamma(\mathcal{L}+\mathcal{M})}{\Gamma(\mathcal{L})\Gamma(\mathcal{M})}\frac{\mathcal{L}}{\mathcal{M}m}\frac{\left(\frac{\mathcal{L}\tau}{\mathcal{M}m}\right)^{\mathcal{L}-1}}{\left(1+\frac{\mathcal{L}\tau}{\mathcal{M}m}\right)^{\mathcal{L}+\mathcal{M}}}\tau\, d\tau \\ &= \left[\frac{\Gamma(\mathcal{L}+\mathcal{M})}{\Gamma(\mathcal{L})\Gamma(\mathcal{M})}\frac{\mathcal{L}}{\mathcal{M}m}\left(\frac{\mathcal{L}\alpha}{\mathcal{M}m}\right)^{\mathcal{L}-1}\right]^2 \\ &\quad\times \alpha^{1-\mathcal{L}}\, I(\alpha, m, \mathcal{L}, \mathcal{M}). \end{aligned} \tag{21}$$

Next, by using the substitution $u = (\mathcal{L}/\mathcal{M}m)\tau$ in (21), it yields

$$\begin{aligned} I(\alpha, m, \mathcal{L}, \mathcal{M}) &= \left(\frac{\mathcal{M}m}{\mathcal{L}}\right)^{2\mathcal{L}} \alpha^{-(\mathcal{L}+\mathcal{M})} \\ &\quad\times \int_0^\infty u^{2\mathcal{L}-1}\left(\frac{1}{\alpha}+u\right)^{-(\mathcal{L}+\mathcal{M})}(1+u)^{-(\mathcal{L}+\mathcal{M})}du. \end{aligned} \tag{22}$$

It has been shown the following relation which links an integral to the Gauss hypergeometric function [32]

$$\begin{aligned} {}_2F_1(a,b;c;z) &= \frac{\Gamma(c)}{\Gamma(b)\Gamma(c-b)} \\ &\quad\times \int_0^\infty t^{-b+c-1}(t+1)^{a-c}(t-z+1)^{-a}dt \end{aligned} \tag{23}$$

with $\Re\mathrm{e}(c) > \Re\mathrm{e}(b) > 0$ and $|\arg(1-z)| < \pi$.

Let $a = \mathcal{L}+\mathcal{M}$, $b = 2\mathcal{M}$, $c = 2a = 2(\mathcal{L}+\mathcal{M})$, $z = 1-(1/\alpha) = (\alpha-1/\alpha)$. By identification between (22) and

(23), one can express I with the Gauss hypergeometric function by

$$I(\alpha,m,\mathcal{L},\mathcal{M}) = \left(\frac{\mathcal{M}m}{\mathcal{L}}\right)^{2\mathcal{L}} \frac{1}{\alpha^{(\mathcal{L}+\mathcal{M})}} \frac{\Gamma(2\mathcal{M})\Gamma(2\mathcal{L})}{\Gamma(2\mathcal{L}+2\mathcal{M})} \times {}_2F_1\left(\mathcal{L}+\mathcal{M}, 2\mathcal{M}; 2(\mathcal{L}+\mathcal{M}); \frac{\alpha-1}{\alpha}\right). \quad (24)$$

By combining (21) and (24), one can obtain the analytical pdf of α by

$$p_\alpha(\alpha) = \left[\frac{\Gamma(\mathcal{L}+\mathcal{M})}{\Gamma(\mathcal{L})\Gamma(\mathcal{M})}\right]^2 \frac{\Gamma(2\mathcal{M})\Gamma(2\mathcal{L})}{\Gamma(2\mathcal{L}+2\mathcal{M})} \frac{1}{\alpha^{\mathcal{M}+1}} \times {}_2F_1\left(\mathcal{L}+\mathcal{M}, 2\mathcal{M}; 2(\mathcal{L}+\mathcal{M}); \frac{\alpha-1}{\alpha}\right). \quad (25)$$

One can rewrite (25) with the Euler Beta function it yields to (10).

Appendix B

If τ_x and τ_y are two correlated random variables, the pdf of the texture ratio α is given by [30, Eq. 6.60]:

$$p_\alpha(\alpha) = \int_0^\infty \tau\, p_{\tau_x\tau_y}(\alpha\tau, \tau)\, d\tau. \quad (26)$$

For correlated Fisher distributed texture, the bivariate Fisher pdf (14) should be used to derive the pdf of α. By replacing its expression in (26), it leads

$$p_\alpha(\alpha) = \frac{\left(\frac{\mathcal{L}_1}{\mathcal{M}_1 m_1}\right)^{\mathcal{L}_1}\left(\frac{\mathcal{L}_2}{\mathcal{M}_2 m_2}\right)^{\mathcal{L}_2}}{B(\mathcal{L}_1,\mathcal{M}_1)\,B(\mathcal{L}_2,\mathcal{L}_1+\mathcal{M}_2)} \times \int_0^\infty \tau(\alpha\tau)^{\mathcal{L}_1-1}(\tau)^{\mathcal{L}_2-1} \times \left(1+\frac{\mathcal{L}_1}{\mathcal{M}_1 m_1}\alpha\tau + \frac{\mathcal{L}_2}{\mathcal{M}_2 m_2}\tau\right)^{-(\mathcal{L}_1+\mathcal{L}_2+\mathcal{M}_2)} \times {}_2F_1(\mathcal{L}_1+\mathcal{L}_2+\mathcal{M}_2, \mathcal{M}_2-\mathcal{M}_1; \mathcal{L}_1+\mathcal{M}_2; w) d\tau \quad (27)$$

with
$w = (\mathcal{L}_1/\mathcal{M}_1 m_1)\alpha\tau/1 + (\mathcal{L}_1\mathcal{M}_1 m_1)\alpha\tau + (\mathcal{L}_2/\mathcal{M}_2 m_2)\tau$.

By replacing in (27) the Gauss hypergeometric function by its expression defined with the Pochhammer symbols ($(a)_n = \Gamma(a+n)/\Gamma(a)$) by

$${}_2F_1(\alpha,\beta;\gamma;t) = \sum_{n=0}^\infty \frac{\Gamma(n+\alpha)}{\Gamma(\alpha)}\frac{\Gamma(n+\beta)}{\Gamma(\beta)}\frac{\Gamma(\gamma)}{\Gamma(n+\gamma)}\frac{t^n}{n!} = \sum_{n=0}^\infty \frac{(\alpha)_n(\beta)_n}{(\gamma)_n}\frac{t^n}{n!} \quad (28)$$

and if we swap the sum and the integral, it yields

$$p_\alpha(\alpha) = \frac{\left(\frac{\mathcal{L}_1}{\mathcal{M}_1 m_1}\right)^{\mathcal{L}_1}\left(\frac{\mathcal{L}_2}{\mathcal{M}_2 m_2}\right)^{\mathcal{L}_2}\alpha^{\mathcal{L}_1-1}}{B(\mathcal{L}_1,\mathcal{M}_1)\,B(\mathcal{L}_2,\mathcal{L}_1+\mathcal{M}_2)} \times \sum_{k=0}^\infty \frac{\Gamma(\mathcal{L}_1+\mathcal{L}_2+\mathcal{M}_2+k)}{\Gamma(\mathcal{L}_1+\mathcal{L}_2+\mathcal{M}_2)}\frac{\Gamma(\mathcal{M}_2-\mathcal{M}_1+k)}{\Gamma(\mathcal{M}_2-\mathcal{M}_1)} \times \frac{\Gamma(\mathcal{L}_1+\mathcal{M}_2)}{\Gamma(\mathcal{L}_1+\mathcal{M}_2+k)}\frac{1}{k!}\,J(k). \quad (29)$$

where $J(k) =$

$$\left(\frac{\mathcal{L}_1\alpha}{\mathcal{M}_1 m_1}\right)^k \int_0^\infty \frac{(\tau)^{\mathcal{L}_1+\mathcal{L}_2+k-1}}{\left(1+\left(\frac{\mathcal{L}_1}{\mathcal{M}_1 m_1}\alpha+\frac{\mathcal{L}_2}{\mathcal{M}_2 m_2}\right)\tau\right)^{\mathcal{L}_1+\mathcal{L}_2+k+\mathcal{M}_2}} d\tau = \left(\frac{\mathcal{L}_1\alpha}{\mathcal{M}_1 m_1}\right)^k K(k). \quad (30)$$

The integral $K(k)$ looks like an integral of a Fisher pdf defined by parameters $m = \mathcal{L}\mathcal{M}((\mathcal{L}_1\mathcal{M}_1 m_1)\alpha + (\mathcal{L}_2\mathcal{M}_2 m_2))$, $\mathcal{L} = \mathcal{L}_1+\mathcal{L}_2+k$ and $\mathcal{M} = \mathcal{M}_2$, it yields

$$K(k) = \int_0^\infty \frac{(\tau)^{\mathcal{L}-1}}{\left(1+\frac{\mathcal{L}\tau}{\mathcal{M}m}\right)^{\mathcal{L}+\mathcal{M}}} d\tau = \frac{\Gamma(\mathcal{L})\Gamma(\mathcal{M})}{\Gamma(\mathcal{L}+\mathcal{M})}\left(\frac{\mathcal{M}m}{\mathcal{L}}\right)^{\mathcal{L}} = \frac{\Gamma(\mathcal{L}_1+\mathcal{L}_2+k)\Gamma(\mathcal{M}_2)}{\Gamma(\mathcal{L}_1+\mathcal{L}_2+k+\mathcal{M}_2)} \times \frac{1}{\left(\frac{\mathcal{L}_1}{\mathcal{M}_1 m_1}\alpha+\frac{\mathcal{L}_2}{\mathcal{M}_2 m_2}\right)^{\mathcal{L}_1+\mathcal{L}_2+k}}. \quad (31)$$

By combining (29), (30), and (31), one can prove that

$$p_\alpha(\alpha) = \frac{R_1^{\mathcal{L}_1}\,R_2^{\mathcal{L}_2}\alpha^{\mathcal{L}_1-1}}{B(\mathcal{L}_1,\mathcal{M}_1)\,B(\mathcal{L}_2,\mathcal{L}_1+\mathcal{M}_2)} \times \frac{\Gamma(\mathcal{L}_1+\mathcal{L}_2)\Gamma(\mathcal{M}_2)}{\Gamma(\mathcal{L}_1+\mathcal{L}_2+\mathcal{M}_2)(R_1\alpha+R_2)^{\mathcal{L}_1+\mathcal{L}_2}} \times \sum_{k=0}^\infty \frac{(\mathcal{M}_2-\mathcal{M}_1)_k(\mathcal{L}_1+\mathcal{L}_2)_k}{(\mathcal{L}_1+\mathcal{M}_2)_k} \times \left[\frac{\left(\frac{\mathcal{L}_1\alpha}{\mathcal{M}_1 m_1}\right)}{(R_1\alpha+R_2)}\right]^k \frac{1}{k!} = \frac{R_1^{\mathcal{L}_1}\,R_2^{\mathcal{L}_2}\alpha^{\mathcal{L}_1-1}}{B(\mathcal{L}_1,\mathcal{M}_1)\,B(\mathcal{L}_2,\mathcal{L}_1+\mathcal{M}_2)}\frac{B(\mathcal{L}_1+\mathcal{L}_2,\mathcal{M}_2)}{(R_1\alpha+R_2)^{\mathcal{L}_1+\mathcal{L}_2}} \times {}_2F_1\left(\mathcal{L}_1+\mathcal{L}_2, \mathcal{M}_2-\mathcal{M}_1; \mathcal{L}_1+\mathcal{M}_2; \frac{\left(\frac{\mathcal{L}_1\alpha}{\mathcal{M}_1 m_1}\right)}{(R_1\alpha+R_2)}\right) \quad (32)$$

with $R_1 = (\mathcal{L}_1/\mathcal{M}_1 m_1)$ and $R_2 = (\mathcal{L}_2/\mathcal{M}_2 m_2)$. It yields to the pdf of the ratio of two correlated Fisher distributed texture shown in (15).

REFERENCES

[1] E. Berthier, H. Vadon, D. Baratoux, Y. Arnaud, C. Vincent, K. L. Feigl, F. Rémy, and B. Legrésy, "Mountain glacier surface motion derived from satellite optical imagery," *Remote Sens. Environ.*, vol. 95, no. 1, pp. 14–28, 2005.

[2] D. Massonnet and T. Rabaute, "Radar interferometry, limits and potential," *IEEE Trans. Geosci. Remote Sens.*, vol. 31, no. 2, pp. 455–464, Mar. 1993.

[3] D. Massonnet and K. Feigl, "RADAR interferometry and its application to changes in the Earth's surface," *Rev. Geophys.*, vol. 36, no. 4, pp. 441–500, 1998.

[4] K. E. Mattar, P. W. Vachon, D. Geudtner, A. L. Gray, I. G. Cumming, and M. Brugman, "Validation of alpine glacier velocity measurements using ERS tandem-mission SAR data," *IEEE Trans. Geosci. Remote Sens.*, vol. 36, no. 3, pp. 974–984, May 1998.

[5] B. T. Rabus and D. R. Fatland, "Comparison of SAR-interferometric and surveyed velocities on a mountain glacier: Black rapids glacier," *J. Glaciol.*, vol. 152, no. 46, pp. 119–128, 2000.

[6] N. Reeh, J. J. Mohr, S. N. Madsen, H. Oerter, and N. S. Gunderstrup, "Three-Dimensional surface velocities of Storstømmen Glacier, Greenland, derived from radar interferometry and ice-sounding radar measurements," *J. Glaciol.*, vol. 49, no. 165, pp. 201–209, 2009.

[7] E. Trouvé, G. Vasile, M. Gay, L. Bombrun, P. Grussenmeyer, T. Landes, J. M. Nicolas, Ph. Bolon, I. Petillot, A. Julea, L. Valet, J. Chanussot, and M. Koehl, "Combining airborne photographs and spaceborne SAR data to monitor temperate glaciers. potentials and limits," *IEEE Trans. Geosci. Remote Sens.*, vol. 45, no. 4, pp. 905–924, Apr. 2007.

[8] R. Fallourd, O. Harant, E. Trouvé, J.-M. Nicolas, F. Tupin, M. Gay, G. Vasile, L. Bombrun, A. Walpersdorf, J. Serafini, N. Cotte, L. Moreau, and P. Bolon, "Monitoring temperate glacier: Combined use of multidate terra SAR-X images and continuous GPS measurements," in *Proc. MultiTemp'09*, Groton, CT, 2009.

[9] I. R. Joughin, R. Kwok, and M. A. Fahnestock, "Interferometric estimation of three-dimensional ice-flow using ascending and descending passes," *IEEE Trans. Geosci. Remote Sens.*, vol. 36, no. 1, pp. 25–37, Jan. 1998.

[10] A. L. Gray, N. Short, K. E. Matter, and K. C. Jezek, "Velocities and ice flux of the filchner ice shelf and its tributaries determined from speckle tracking interferometry," *Can. J. Remote Sens.*, vol. 27, no. 3, pp. 193–206, 2001.

[11] N. H. Short and A. L. Gray, "Potential for RADARSAT-2 interfermerometry: Glacier monitoring using speckle tracking," *Can. J. Remote Sens.*, vol. 30, no. 3, pp. 504–509, 2004.

[12] F. Serafino, "SAR image coregistration based on isolated point scatterers," *IEEE Geosci. Remote Sens. Lett.*, vol. 3, no. 3, pp. 354–358, Jul. 2006.

[13] R. Michel, J. P. Avouac, and J. Taboury, "Measuring ground displacements from SAR amplitude images: Application to the landers earthquake," *Geophys. Res. Lett.*, vol. 26, no. 7, pp. 875–878, 1999.

[14] T. Strozzi, A. Luckman, T. Murray, U. Wegmuller, and C. L. Werner, "Glacier motion estimation using SAR offset-tracking procedures," *IEEE Trans. Geosci. Remote Sens.*, vol. 40, no. 11, pp. 2384–2391, Nov. 2002.

[15] E. Erten, A. Reigber, O. Hellwich, and P. Prats, "Glacier velocity monitoring by maximum likelihood texture tracking," *IEEE Trans. Geosci. Remote Sens.*, vol. 47, no. 2, pp. 394–405, Feb. 2009.

[16] G. Vasile, J.-P. Ovarlez, F. Pascal, and C. Tison, "Coherency matrix estimation of heterogeneous clutter in high resolution polarimetric SAR images," *IEEE Trans. Geosci. Remote Sens.*, vol. 48, no. 4, pp. 1809–1826, Apr. 2010.

[17] L. Bombrun, G. Vasile, M. Gay, and F. Totir, "Hierarchical segmentation of polarimetric SAR images using heterogeneous clutter models," *IEEE Trans. Geosci. Remote Sens.*, vol. 49, no. 2, pp. 726–737, Feb. 2011.

[18] K. T. Fang, S. Kotz, and K. W. Ng, *Symmetric Multivariate and Related Distributions*. London, U.K.: Chapman & Hall, 1990.

[19] S. Zozor and C. Vignat, "Some results on the denoising problem in the elliptically distributed context," *IEEE Trans. Signal Process.*, vol. 58, no. 1, pp. 134–150, Jan. 2010.

[20] F. Pascal, Y. Chitour, J. P. Ovarlez, P. Forster, and P. Larzabal, "Covariance structure maximum-likelihood estimates in compound gaussian noise: Existence and algorithm analysis," *IEEE Trans. Signal Process.*, vol. 56, no. 1, pp. 34–48, Jan. 2008.

[21] F. Pascal, P. Forster, J. P. Ovarlez, and P. Larzabal, "Performance analysis of covariance matrix estimates in impulsive noise," *IEEE Trans. Signal Process.*, vol. 56, no. 6, pp. 2206–2216, Jun. 2008.

[22] J. S. Lee, D. L. Schuler, R. H. Lang, and K. J. Ranson, "K-distribution for multi-look processed polarimetric SAR imagery," in *Proc. Geosci. Remote Sens., IGARSS'94*, Pasadena, CA, 1994, pp. 2179–2181.

[23] C. C. Freitas, A. C. Frery, and A. H. Correia, "The polarimetric G distribution for SAR data analysis," *Environmetrics*, vol. 16, pp. 13–31, 2005.

[24] L. Bombrun and J.-M. Beaulieu, "Fisher distribution for texture modeling of polarimetric SAR data," *IEEE Geosci. Remote Sens. Lett.*, vol. 5, no. 3, pp. 512–516, Jul. 2008.

[25] C. Tison, J.-M. Nicolas, F. Tupin, and H. Maître, "A new statistical model for markovian classification of urban areas in high-resolution SAR images," *IEEE Trans. Geosci. Remote Sens.*, vol. 42, no. 10, pp. 2046–2057, Oct. 2004.

[26] J.-M. Nicolas, "Introduction aux Statistiques de Deuxième Espèce: Applications des Logs-moments et des Logs-cumulants á l'Analyse des lois d'Images Radar," *Traitement du Signal*, vol. 19, no. 3, pp. 139–167, 2002.

[27] J.-M. Nicolas, Application de la Transformée de Mellin: étude des Lois Statistiques de l' Imagerie Cohérente Rapport de recherche, 2006D010, 2006.

[28] M. G. Strintzis and I. Kokkinidis, "Maximum likelihood motion estimation in ultrasound image sequences," *IEEE Signal Process. Lett.*, vol. 4, no. 6, pp. 156–157, Jun. 1997.

[29] R. Bamler, "Interferometric stereo radargrammetry: Absolute height determination from ERS-ENVISAT interferograms," in *Proc. Geosci. Remote Sens., IGARSS'00*, 2000, vol. 2, pp. 742–745.

[30] A. Papoulis, *Probability, Random Variables, and Stochastic Processes*, 4th ed. New York: McGraw-Hill, 2002.

[31] A. H. El-Bassiouny and M. Jones, "A bivariate F distribution with marginals on arbitrary numerator and denominator degrees of freedom, and related bivariate beta and t distributions," *Statist. Methods Applicat.* , pp. 465–481, 2008.

[32] M. Abramowitz and I. A. Stegun, *Handbook of Mathematical Functions With Formulas, Graphs, and Mathematical Tables*. New York: Dover, 1964.

[33] Y. Delignon, "Etude statistique d'images radar de la surface de la mer," These de Doctorat, Univ. de Rennes I, Paris, France, 1993.

Olivier Harant was born in 1982. He received the Engineer degree in electrical engineering from the Ecole Suprieure de Chimie Physique et Electronique, Lyon, France, in 2008. He is currently working toward the Ph.D. degree in the SAR Polarimetry, Holography, Interferometry, and Radargrammetry (SAPHIR) Team, Institut of Electronic and Telecommunication, Rennes, in collaboration with the Grenoble Image sPeech and Automatic laboratory (GIPSA-Lab).

His research interests include information modeling in polarimetric SAR images and glaciers monitoring.

Lionel Bombrun (S'06–M'09) was born in Tournon, France, in 1982. He received the M.S. and Ph.D. degrees in signal, image, speech, and telecommunications from the Grenoble National Polytechnic Institute (INPG), Grenoble, France, in 2005 and 2008, respectively.

In 2008, he was a Teaching Assistant at Phelma, Grenoble. From 2009 to 2010, he was a Postdoctoral Fellow from the French National Council for Scientific Research (CNRS) between the Grenoble Image Speech Signal Automatics Laboratory and SONDRA, Gif-sur-Yvette, France. Since October 2010, he has been a Postdoctoral Fellow at the IMS Laboratory. His research interests include signal and image processing, texture analysis, synthetic aperture radar remote sensing, polarimetry, and interferometry.

Gabriel Vasile (S'06–M'07) received the M.Eng. degree in electrical engineering and computer science and the M.S. degree in image, shapes, and artificial intelligence from the POLITEHNICA University, Bucharest, Romania, in 2003 and 2004, respectively, and the Ph.D. degree in signal and image processing from Savoie University, Annecy, France, in 2007.

From 2007 to 2008, he was a Postdoctoral Fellow with the French Space Agency (CNES) and was with the French Aerospace Laboratory (ONERA), Palaiseau, France. In 2008, he joined the French National Council for Scientific Research (CNRS), where he is currently a Research Scientist and a member of the Grenoble Image Speech Signal Automatics Laboratory, Grenoble, France. His research interests include signal and image processing, synthetic aperture radar remote sensing, polarimetry, and interferometry.

Laurent Ferro-Famil (M'00) received the laurea degree in electronics systems and computer engineering, the M.S. degree in electronics, and the Ph.D. degree, all from the University of Nantes, Nantes, France, in 1996, 1996, and 2000, respectively.

Since 2001, he has been an Assistant Professor at the University of Rennes I, Rennes, France. He is a member of the Radar Polarimetry Remote Sensing Group, Institute of Electronics and Telecommunications of Rennes (IETR). His current activities in education concern analog electronics, digital communications microwave theory, and polarimetric radar imaging. He is especially interested in SAR signal processing, radar polarimetry theory, and natural media remote sensing from polarimetric interferometric SAR data, with application to segmentation, classification, electromagnetic scattering modeling, physical parameter inversion, and time–frequency analysis.

Michel Gay (M'10) received the Engineer degree in electrical engineering from the Institut des Sciences de l'Ingéieur de Montpellier, Montpellier, France, in 1987 and the Ph.D. degree in physics from the University Joseph Fourier, Grenoble, France, in 1999.

From 1979 to 1985, he worked with the Botanic Institute and with the local education authority of Montpellier. From 1988 to 2003, he was with Cemagref Grenoble, where he worked on electrical engineering for environmental applications. Since 2004, he has been a Research Engineer with the Grenoble Image Speech Signal Automatic Laboratory, Institut National Polytechnique de Grenoble, Centre National de la Recherche Scientifique, Saint-Martin-d'Hères, France. His current research interests include remote sensing, synthetic aperture radar (SAR) image processing, and survey of Alpine glaciers. He has been Co-Manager of four National Scientific projects and of three international projects and Leader Project of one international project.

Dr. Gay is a member of the IEEE Geoscience Remote Sensing Society.